Available online at www.sciencedirect.com
SCIENCE DIRECT®
PERGAMON
International Journal of Heat and Mass Transfer 46 (2003) 1641–1652
International Journal of HEAT and MASS TRANSFER
www.elsevier.com/locate/ijhmt

Effect of thermocapillary convection in an industrial Czochralski crucible: numerical simulation

V. Kumar [a,*], G. Biswas [b], G. Brenner [a], F. Durst [a]

[a] Institute of Fluid Mechanics, LSTM, University of Erlangen-Nürnberg, Cauerstr. 4, D-91058 Erlangen, Germany
[b] Department of Mechanical Engineering, Indian Institute of Technology, Kanpur-208016, India

Received 9 April 2002; received in revised form 3 September 2002

Abstract

The influence of thermocapillary or Marangoni convection on the growth of silicon crystals is investigated in an industrial Czochralski crucible using a quasi direct numerical simulations approach. An optimized parallel-vector block-structured finite volume Navier–Stokes equations solver is extended to include the effects of thermocapillary convection. Owing to the presence of surface tension gradients, the magnitude of the radial velocity towards the crystal becomes high at the free surface. Consequently, the temperature along the free surface is increased. The thermocapillary convection reduces the temperature fluctuations below the crystal and the free surface of the melt. However, below the crystal, the turbulent kinetic energy, k, is higher at different melt depths when the thermocapillary effect is taken into account. It is necessary to study the above-mentioned effects of surface tension driven convection since they influence the quality of the crystal.

Keywords: Crystal growth; Natural convection; Thermocapillary

1. Introduction

The flow in a Czochralski (Cz) melt is governed by the interaction of various forces, namely buoyancy, centrifugal, Coriolis and surface tension [1–4]. The transport of heat and momentum takes place at different length and time scales, which makes the process very difficult to characterise. With the increasing demand for large-diameter crystals, which requires bigger crucibles, the magnitudes of different interacting forces increase and therefore the flow in the melt becomes turbulent [5,6]. As a consequence, it becomes very challenging to compute and measure the average and fluctuating quantities. The flow influences the quality of the crystal through the convective heat and mass transport. The surface tension induced flow or thermocapillary convection influences the transport of heat and mass near the region in the melt where the crystal grows [7,8]. Therefore, it influences the quality of the crystal. The effect of thermocapillary convection on Cz crystal growth for high-Prandtl number (Pr) fluids has been the subject of many investigations [9–14]. In contrast, the effects of Marangoni convection on low-Pr fluids, such as silicon (Si), have not been studied sufficiently. Moreover, the time-dependent three-dimensional (3D) simulations require high-computational power and time, which often makes the full simulation unaffordable.

The thermocapillary flow or the flow induced by the change in surface tension of the fluid due to the presence of temperature gradients gives rise to the Marangoni-Bérnard instability in the melt. Ristorcelli and Lumley [5] discussed various types of instabilities in Cz crystal growth. The instabilities in the melt give rise to an asymmetric and time-dependent thermal field. The instability occurs in the melt more easily if thermocapillary forces are present [15]. Azami et al. [7] observed dark patterns, so called *spoke patterns*, on the surface of an Si melt by using CCD images and they attributed these patterns to surface tension forces. The influence of

* Corresponding author. Tel.: +49-9131-852-8279; fax: +49-9131-852-9503.
E-mail address: vivek@lstm.uni-erlangen.de (V. Kumar).

0017-9310/03/$ - see front matter
PII: S0017-9310(02)00457-X

Nomenclature

c_p	specific heat
g	acceleration due to gravity
Gr	Grashof number
H_c	height of the melt in the crucible
k	turbulent kinetic energy
Ma	Marangoni number
p	pressure
Pr	Prandtl number
Q	source term in conservation equations
r	radial coordinate
$\mathbf{r}$	radial position vector
R_c	radius of the crucible
R_s	radius of the crystal
Re	Reynolds number
t	time
T	temperature
T_{ref}	reference temperature
T'	temperature fluctuation
$\overline{T}$	time-averaged temperature
u_i	ith Cartesian velocity vector
$\overline{v}_r$	time-averaged radial velocity
x_i	ith Cartesian coordinate
z	axial coordinate

Greek symbols

α	thermal diffusivity
β	thermal expansion coefficient
ϵ	emissivity
ϕ	general transport quantity
Φ	energy loss due to dissipation
γ	temperature coefficient of surface tension
Γ	molecular diffusion coefficient
η	normal to free surface
λ	thermal conductivity
μ	dynamic viscosity
ν	kinematic viscosity
ω	angular velocity
Ω	rotation rate in rpm
ρ	density
ρ_{ref}	reference density
σ	surface tension
σ_{st}	Stefan–Boltzmann constant
τ	shear stress
θ	azimuthal coordinate
ξ, ζ	tangential coordinates

Subscripts

c	crucible
s	crystal
env	environment
hor	horizontal
max	maximum
r	radial
ref	reference

Marangoni-Bérnard flow on the transport of oxygen in an Si melt has also been investigated [16]. Kakimoto and Ozoe [17] concluded that the surface tension driven flow has to be taken into account in the calculation of oxygen transfer in the melt. Their 3D simulations reveal that the residence time of the melt at the free surface is increased and consequently the rate of evaporation of oxygen is overestimated if the thermocapillary convection is neglected. Recently, Li et al. [18] performed two-dimensional (2D) axi-symmetric and steady-state computations in an Si furnace and investigated the effect of surface tension gradients on the flow field and on oxygen concentration in the melt.

For a high-Pr fluid, where convection mainly controls the transport of heat, the thermocapillary effect is more significant. Lamprecht et al. [19] reported from their experiments that the flow velocity at the free surface of a high-Pr melt is approximately 20 times higher than the surface velocity for the case when the thermocapillary force is suppressed. Galazka and Wilke [12] performed 2D simulations in a YAG melt and concluded that the superposition of the thermocapillary force over the buoyancy force causes a change in the shape of the crystal-melt interface. Hirata and Fukuda [20] studied the effect of the thermal buoyancy, the thermocapillary effect and forced convection on the shape of the growth interface. According to them, if the natural convection dominates over the forced convection, flow near the surface is strongly directed towards the center of the crucible and therefore the crystal-melt interface is convex in the downward direction. Jing et al. [10] indicated in their simulations that the temperature and velocity fields become time-dependent even at a low Grashof number (Gr) in the presence of Marangoni convection. In another study by Jing et al. [11], it was concluded that the Marangoni instability is the cause of the spoke patterns at the free surface of $LiNbO_3$ melt.

This work was an attempt to elucidate the effect of thermocapillary or Marangoni convection on the mean and fluctuating temperature and velocity fields in a Si melt during the growth of an Si single crystal. Although the mean temperature field in an Si melt is not expected to be influenced much by the thermocapillary force, the fluctuating temperature and velocity fields are strongly influenced by the effect of Marangoni convection [21]. Wagner and Friedrich [21,22] performed the direct numerical simulation of a cylindrical Cz configuration under the influence of Marangoni convection. In their

simulations, the Marangoni number (Ma), was 3.6×10^4. They observed an increase of 58% in the magnitude of the inward radial surface velocity in the presence of Marangoni convection.

2. Statement of the problem

The geometry of the crucible and the local coordinate system at a free surface are shown in Fig. 1(a) and (b). The crucible has a radius $R_c = 18$ cm and height $H_c = 10$ cm. The radius of the crystal $R_s = 5.2$ cm. The radii of curvature are $R_1 = 39.2$ cm and $R_2 = 4.3$ cm. The mass of the Si ingot is 20 kg. The crystal is vertically pulled upwards at an average rate of 2 mm/min. The shape of the crystal-melt interface is considered to be flat in the simulations. The crystal and the crucible are rotated in opposite directions. The rotation rates of the crystal, Ω_s, and the crucible, Ω_c, are 20 and −2 rpm, respectively. The negative sign here indicates that the rotation is in an anti-clockwise direction.

In order to retain the advantages of the structured grids, a grid-mesh with six geometrical blocks was employed for the simulations. The Navier–Stokes equations solver is parallelized by assigning the geometrical blocks to the different processors during the computation. The skewness of the grid for such a cylindrical geometry can be well controlled by this block-structured approach [23]. When block-structured grids are used, the pressure, pressure correction, flux, velocity and temperature must be exchanged between two neighboring blocks. Fig. 2 shows a schematic diagram of the block-structured grid used for the present simulations, which consists of 10^6 grid points. The center of the crucible was mapped with an almost rectangular block. The outer region was divided into four symmetrical blocks and a sixth block was created to fit the ellipsoidal bottom of the crucible. The thermo-physical properties of Si used in the simulations are provided in Table 1 [23]. The free surface of the melt is considered to be flat and forces due to the motion of the gas above the melt are neglected.

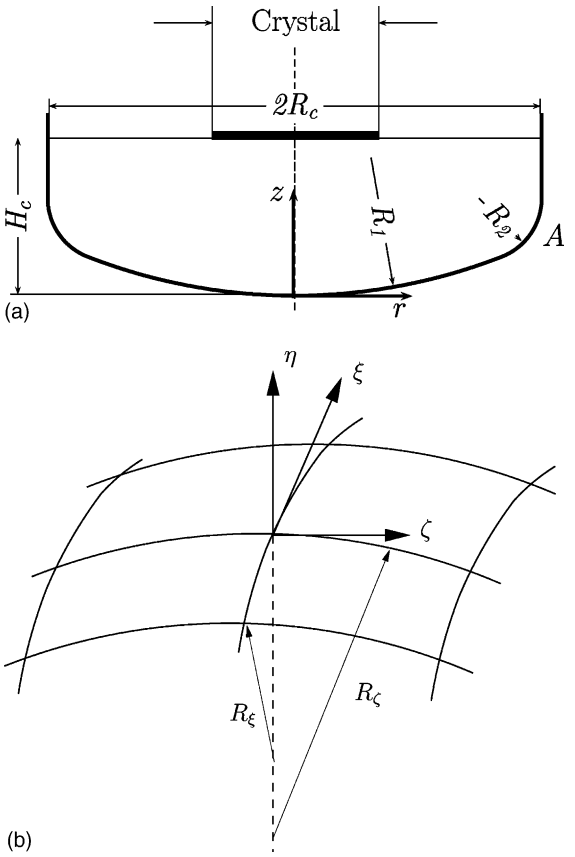

Fig. 1. (a) The geometry of the industrial Cz crucible and (b) local coordinates (ξ, η, ζ) on a free surface.

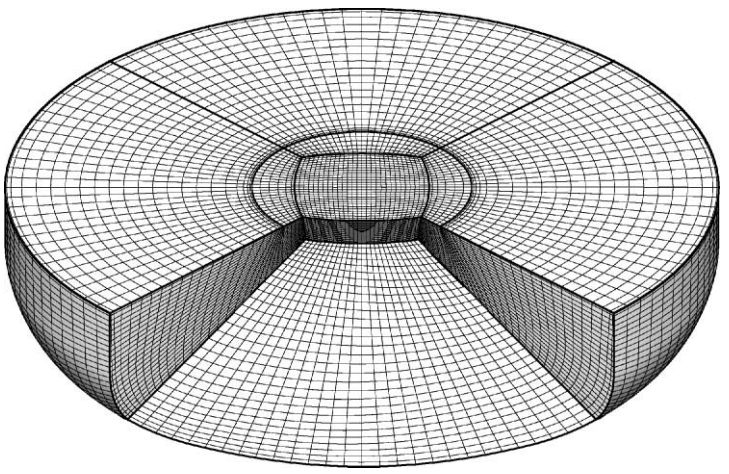

Fig. 2. The block-structured grid-mesh generated for the simulation.

Table 1
Thermo-physical properties of Si melt

Symbol	Value	Unit
T_{ref}	1700	K
ρ_{ref}	2570.0	kg/m^3
μ	7.75×10^{-4}	N s/m^2
β	1.4×10^{-4}	K^{-1}
λ	66.9	W/m K
c_p	915.0	J/kg K
v	3.02×10^{-7}	m^2/s
α	2.85×10^{-5}	m^2/s
γ	-4.3×10^{-4}	N/m K
ϵ	0.3	–
Pr	0.011	–

Based on the maximum temperature difference inside the melt, ($Gr = g\beta H_c^3 \Delta T_{max}/v^2$) is equal to 4.1×10^8. ($Ma = -d\sigma/dT\, Pr \Delta T_{hor}(R_c - R_s)/\rho v^2$) is calculated based on the measured value of temperature difference on the free surface, i.e. between the top of the crucible outer wall and the solid crystal ($\Delta T_{hor} = 17.0$ K) [24] and is equal to 1.2×10^5. The reported values of the temperature coefficient of surface tension, $\gamma = -d\sigma/dT$, lie between -1.6×10^{-5} and -7.5×10^{-4} N/m K [7,25], where σ is the surface tension. In the simulations performed in this work, the upper value of γ was taken from Ref. [26]. The Reynolds number based on crucible rotation, $Re = \Omega_c R_c^2/v$, is equal to 3176.

3. Mathematical formulation

The transient flow and thermal fields in the melt are described by 3D time-dependent continuity, momentum and energy conservation equations. The Boussinesq approximation for a Newtonian fluid was taken into account.

3.1. Conservation equations

The conservation equations can be written in the form of a general transport equation:

$$\frac{\partial}{\partial t}(\rho\phi) + \frac{\partial}{\partial x_i}(\rho u_i \phi) = \frac{\partial}{\partial x_i}\left(\Gamma \frac{\partial \phi}{\partial x_i}\right) + Q_j \tag{1}$$

where ϕ is the general transport quantity, Γ the molecular diffusion coefficient and Q_j the source term of the conservation equations as defined in Table 2, where g_j [0,0,−9.81] is the gravity vector, p the reference pressure, β the coefficient of volumetric expansion, T_{ref} the reference temperature for the Boussinesq approximation, $\Phi = \mu(\partial u_i/\partial x_j + \partial u_j/\partial x_i)\partial u_i/\partial x_j$ the energy loss due to dissipation and $B_i = -\rho[2\omega \times \mathbf{u} + \omega \times (\omega \times \mathbf{r})]$ are the centrifugal and Coriolis forces due to the rotation of the crucible. The additional terms, Coriolis and centrifugal forces, appear in the momentum equations because the equations are written for a non-inertial reference frame. The continuity and energy equations remain unchanged.

Table 2
Variables in general transport equation

Conserved quantity	ϕ	Γ	Q_j
Mass	1	1	0
Momentum	u_j	μ	$-\frac{\partial p}{\partial x_j} + \rho_{ref} g_j \beta (T - T_{ref}) + B_i$
Thermal energy	T	$\frac{\lambda}{c_p}$	$\frac{\Phi}{c_p}$

3.2. Boundary and initial conditions

For computing the flow field, the no-slip boundary condition was applied to the crystal-melt interface and the crucible wall. The computations were performed in a rotating reference frame with a velocity equal to the rotation rate of the crucible (Ω_c) of −2 rpm. Therefore, all three components of the velocity vector were set zero at the crucible wall. At the crystal-melt interface, the velocity $\mathbf{u} = (\mathbf{\Omega_c} + \mathbf{\Omega_s}) \times \mathbf{r}$ was prescribed, where $\mathbf{r}$ is the radial position vector. In order to investigate the influence of thermocapillary convection, the simulations were performed with and without the thermocapillary effect. For the case when the the surface tension forces are neglected, all components of shear stress tensor are set equal to zero, i.e. $\tau_{ij} = 0$, and with the thermocapillary effect, the boundary conditions are

$$\begin{aligned}
\tau_{\eta\eta} &= -2\mu \frac{\partial u_\eta}{\partial \eta} = 0 \\
\tau_{\eta\xi} &= -\mu \frac{\partial u_\xi}{\partial \eta} = -\frac{\partial \sigma}{\partial \xi} = -\frac{d\sigma}{dT}\frac{\partial T}{\partial \xi} \\
\tau_{\eta\zeta} &= -\mu \frac{\partial u_\zeta}{\partial \eta} = -\frac{\partial \sigma}{\partial \zeta} = -\frac{d\sigma}{dT}\frac{\partial T}{\partial \zeta}
\end{aligned} \tag{2}$$

where ξ, η and ζ are local coordinates for the each control volume node at the free surface; ξ and ζ are two local tangential directions and η is orthogonal to both ξ and ζ. The local coordinates ξ, η and ζ at a free surface are shown in Fig. 1(b). The pressure in the gas phase above the melt and in the melt are considered to be equal and the radii of curvature of the free surface (R_ζ and R_ξ) are assumed to be infinite in the above boundary conditions.

For the thermal boundary conditions, the measured temperature from the work of Gräbner et al. [24] was prescribed at the crucible wall. The measured data are fitted into a ninth-order polynomial as function of the crucible height and shown in Fig. 3. A fixed temperature of 1687 K, equal to the melting temperature of Si was prescribed at the crystal-melt interface. At the free surface of the melt, the radiation loss was taken into account in the following way:

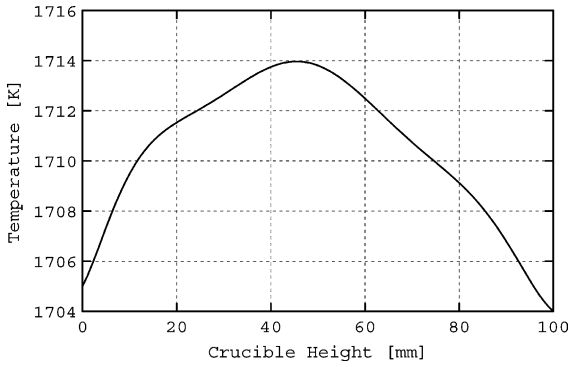

Fig. 3. Temperature profile at the crucible wall as a function of crucible height.

$$\lambda \nabla T = \sigma_{st} \epsilon (T^4 - T_{env}^4) \tag{3}$$

where λ is the thermal conductivity of the melt, ∇T the normal temperature gradient at the free surface, σ_{st} the Stefan–Boltzmann coefficient, T the surface temperature and $T_{env} = 1600$ K the surrounding temperature.

In order to save on the computational time for development of the initial thermal field in the crucible, the temperature was initialized by solving only the steady-state thermal energy equation with appropriate boundary conditions. This solution was used as an initial guess for the time-dependent calculations for both the temperature and the velocity field. The crucible was rotated with a constant speed and initially the flow of the melt was not influenced by any force of external origin. Therefore, a uniform solid body rotation was used as an initial condition for the velocity field in the melt.

4. Solution method

The finite volume method was used for the discretization of the conservation equations. The computations were performed for boundary fitted curvilinear grids. The multigrid technique was adopted to accelerate the rate of convergence. At each time step, the residual of each variable was brought down to 5–6 orders of magnitude to achieve convergence. Multigrid techniques are very sensitive to nuances of the implementations in a numerical code [27]. Therefore, the implementation of an implicit boundary condition, such as the Marangoni boundary condition, together with the multigrid technique, is not straight forward. It must be kept in mind that during the restriction and prolongation cycles, the values of the velocities at the boundary grid nodes must not be interpolated. The temporal discretization was performed adopting a second-order fully implicit scheme. The second-order implicit scheme may produce oscillatory results for high-Courant number. Therefore a small time step Δt was employed. A time step of 0.01 s was used and the data were sampled for time averaging after every two time steps. The averaged and fluctuating quantities were computed with these sampled data. Under-relaxation factors [28] of 0.7, 0.5 and 0.9 were applied for the velocity components, pressure and temperature, respectively. The Simple algorithm [28] was used to solve the coupled velocity and pressure fields.

The discretization of the general transport Eq. (1) for the variable ϕ on a 3D grid-mesh with N control volumes results in a system of equations of the form

$$C\phi = \mathbf{S} \tag{4}$$

where C is an $N \times N$ coefficient matrix, ϕ the unknown column vector of the dependent variables and $\mathbf{S}$ the resultant vector of dimension N. The discretized conservation equations were solved iteratively adopting the strongly implicit procedure (SIP) of Stone [29]. A flow diagram of the solution algorithm is given in Fig. 4. The time-dependent computations for a grid-mesh with 10^6 grid nodes take a considerable time even on vector/parallel computing machines, although the code used for the simulations, FASTEST-3D [30], is highly optimized for these computer architectures.

5. Results and discussions

In this section, the results obtained from the time-dependent simulations are presented. The velocity and temperature fields are analyzed and the influence of thermocapillary forces on the transport of heat and momentum is discussed.

5.1. Time-averaged velocity field

The instantaneous flow field in the Si melt is asymmetric and highly random [31], and therefore it is difficult to predict any definite trend from this highly random flow field. Therefore, to filter out the fluctuations in the melt and to have an insight into the effect of the various pertinent input parameters, the velocity field was statistically averaged by sampling the data after every second time step. During the simulations, time-averaging started 60 s after the beginning of the simulation in order to exclude the influence of the initial quiescent velocity field.

Fig. 5 shows the time-averaged velocity field for the cases with and without thermocapillary forces. The method which was adopted to illustrate the velocity fields here is called the line integral convolution (LIC) technique, developed by Cabral and Leedom [32]. A high-velocity free surface motion is observed due to the thermocapillary effect. Usually the crucible in a Cz furnace is heated along the periphery. The outer bottom region of the crucible attains a very high temperature. Typically, the temperature is highest at the junction

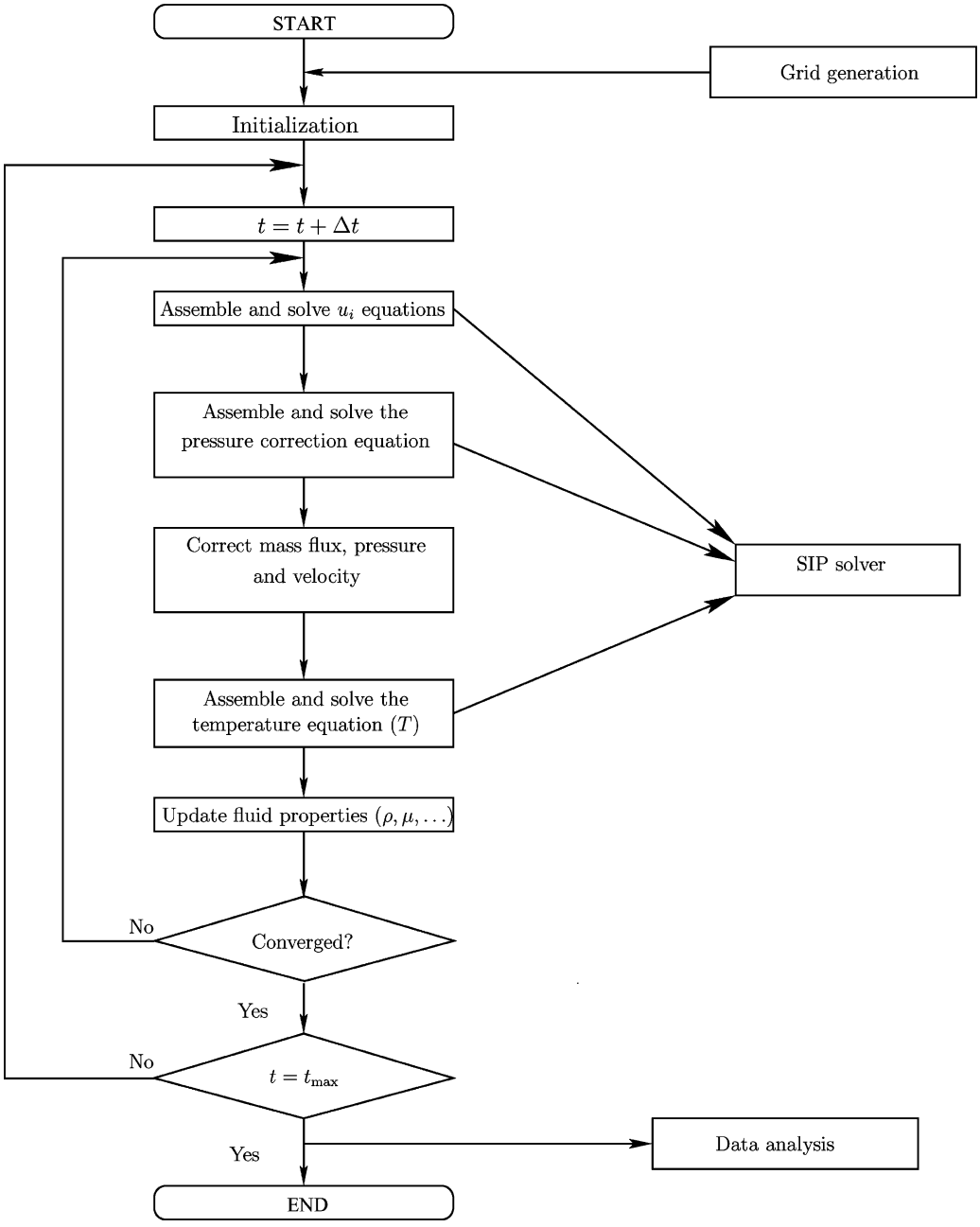

Fig. 4. Flow chart of the iterative solution algorithm.

between the bottom wall and the side wall of the crucible (shown by A in Fig. 1(a)). The high-temperature regime around this location initiates the buoyancy driven flow and there is a rising motion along the crucible wall due to the buoyancy effect. In both cases, with and without the surface tension forces, the liquid tends to rise near the heated side wall and falls near the center of the crucible. In the absence of the thermocapillary effect, there is a vortex loop close to the interface of the crystal. The cooler stream comes down from the crystal, becomes locally heated at the bottom of the crucible and rises to the top surface. The centrifugal force resulting from the crystal rotation, imparts its effect in the radial direction. The radially outward motion interacts with the radially inward flow from the side wall of the crucible and creates an induced vortex (Fig. 5(a)). Fig. 5(a)

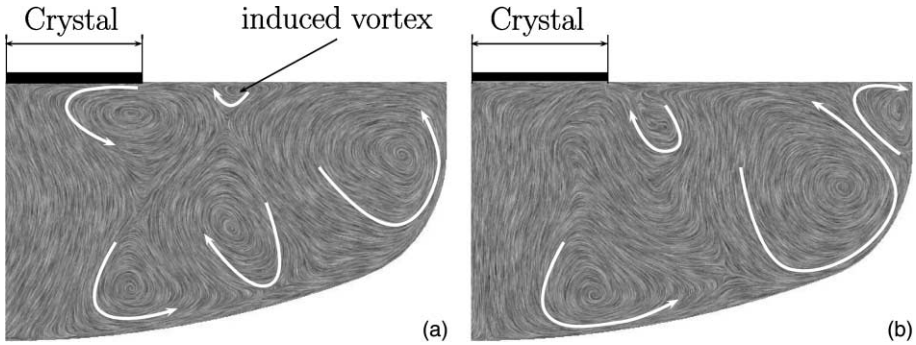

Fig. 5. Time-averaged velocity field (LIC) on a half vertical cut through the crucible (a) without and (b) with thermocapillary forces.

also illustrates that the recirculation zone near the crystal and the vortical flow at the edge of the crucible extend their influence and the liquid trapped between these two vortex systems is rolled up. This rolled vortex, together with its left and right neighbors, forms Rayleigh–Bérnard like cells. In the presence of Marangoni convection, the inward radial velocity of the free surface plays a major role in determining the flow structure inside the crucible. The induced vortex, described earlier, is further strengthened and consequently the cell underneath the crystal changes its pattern (Fig. 5(b)). The plume initiated at the central bottom part of the crucible (underneath the crystal) does not extend to the top surface. The relatively cooler stream coming from the top interacts with the plume and generates a Rayleigh–Bérnard cell near the bottom wall of the crucible.

The *Pr* of a melt plays an important role in determining the growth of the crystal. At high values of the *Pr*, either the momentum boundary layer is of the same order of magnitude as the thermal boundary layer or the former is larger than the latter. Thermal convection flows are concentrated in the thermal boundary layer regions. On the other hand, at low values of the *Pr*, the thermal boundary layer is much larger than the momentum boundary layer and the influence of the applied thermal gradients is felt over a greater volume of liquid. As a result, an early transitions may be induced in the melt of low *Pr*-fluids.

The thermocapillary flow is induced by the the surface tension gradients at the free surface. However, it is envisaged to influence the flow pattern even at a few millimeters below the free surface of the melt. Therefore, the azimuthal and time-averaged radial velocities are plotted along the radial distance at $z = 99$ and 98 mm below the free surface of the melt as shown in Fig. 6. At both positions, the average radial velocity changes its sign near the side wall of the crucible and the change in sign is commensurate with the presence of a 3D vortex in this region. However, the LIC representation of Fig. 5(a) smears out this considerably small 3D vortex. The magnitude of the radial velocity near the side wall is

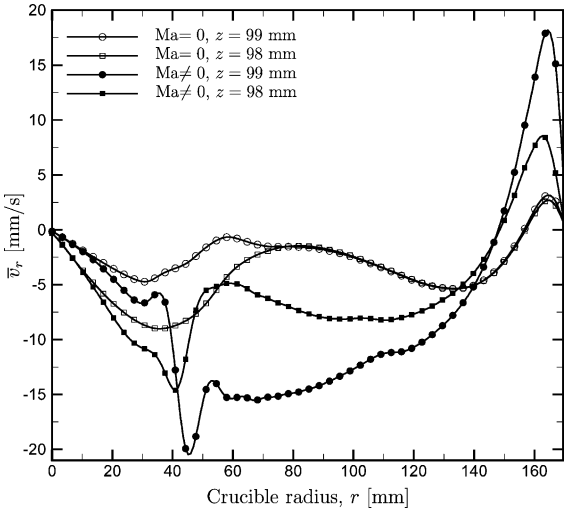

Fig. 6. Azimuthal- and time-averaged radial velocity $\overline{v}_r$ plotted at different melt heights for the cases with and without the thermocapillary effect.

higher when the thermocapillary forces are included and therefore the vortex near the upper corner of the crucible influences the orientation of the largest buoyancy plume in the melt (also see Fig. 5(b)). The creation of this vortex can be attributed to the buoyancy plume rising from the outer bottom of the crucible. The plume develops into a localized hot spot (ring) on the free surface. This circular zone sets up temperature gradients in the radially opposite directions. The temperature gradient between this zone and the cold crystal is responsible for the free surface flow that has already been discussed. However, the difference in temperature between this zone and the relatively cooler crucible wall culminates in a 3D motion that persists at the upper corner. At a distance of about 60 mm from the center of the crucible, there is a significant difference in the radial velocities for the cases with and without thermocapillary convection at $z = 99$ mm. This difference in the radial velocity can be attributed to the forced convection due

to the crystal rotation. Here the centrifugal vortex balances the buoyancy driven vortex. On the other hand, with the inclusion of surface tension driven forces, the overall flow is radially inward along the free surface of the melt. It is also apparent from Fig. 5(b) that the effect of the thermocapillary convection is reduced significantly towards the depth of the melt. The mean time-averaged radial velocities at $z = 99$ mm are 7.51 and 2.31 mm/s for the cases with and without the thermocapillary effect, respectively. Below the crystal, the flow is directed towards the center at both heights ($z = 98$ and 99 mm) irrespective of the presence of thermocapillary forces. The maximum negative velocity occurs at a radial distance about 35–45 mm for all cases. The inward radial velocity, which is the outcome of the overall recirculating flow pattern due to thermal buoyancy, is further influenced by the Marangoni convection and the magnitude of the inward radial velocity becomes higher. It attains the highest value at the free surface near the crystal.

Fig. 7 shows the time-averaged velocity vectors on a horizontal section, at the center of the first control volume underneath the free surface, with and without thermocapillary forces. Every second vector is plotted on the horizontal plane and in both cases. The rotation of the crucible and the thermal buoyancy generate motion in the melt in the r and θ directions. The resulting Coriolis force brings about a significant mixing in the tangential direction in order to avoid spoke patterns as observed by Azami et al. [7]. However, the Marangoni effect culminates in a strong radially inward motion of the melt. If one approaches the growing crystal from the periphery of the crucible, the radial velocity shows a progressively higher magnitude on the free surface at the shorter radial distances from the crystal in order to satisfy the conservation of mass. This effect is more prominent for the case with thermocapillary force. The higher mass flow leads to a higher surface temperature gradient at the edge of the crystal. The effect of this higher temperature gradient will be discussed in a subsequent section.

5.2. Time-averaged temperature field

Fig. 8(a) and (b) show the time-averaged temperature field on a vertical plane for the cases with and without the effect of thermocapillary forces. From both plots, it can be seen that there is an increase in temperature from the inner top location of the crucible to the outer bottom location. In the presence of the thermocapillary effect, the temperature gradient along the free surface is reduced. A higher temperature gradient exists near the crystal edge for the case with the Marangoni effect as compared with the case without the Marangoni effect. From this typical behavior of the Marangoni convection, it can be inferred that the numerical grid near the crystal should be refined locally in order to compute accurately the surface velocity. In the absence of proper grid refinement, the surface velocity can be unrealistically high in the first control volume next to the crystal. Owing to the thermocapillary convection, the isotherms penetrate deeper inside the crucible and create a steeper temperature gradient at the inner bottom of the crucible

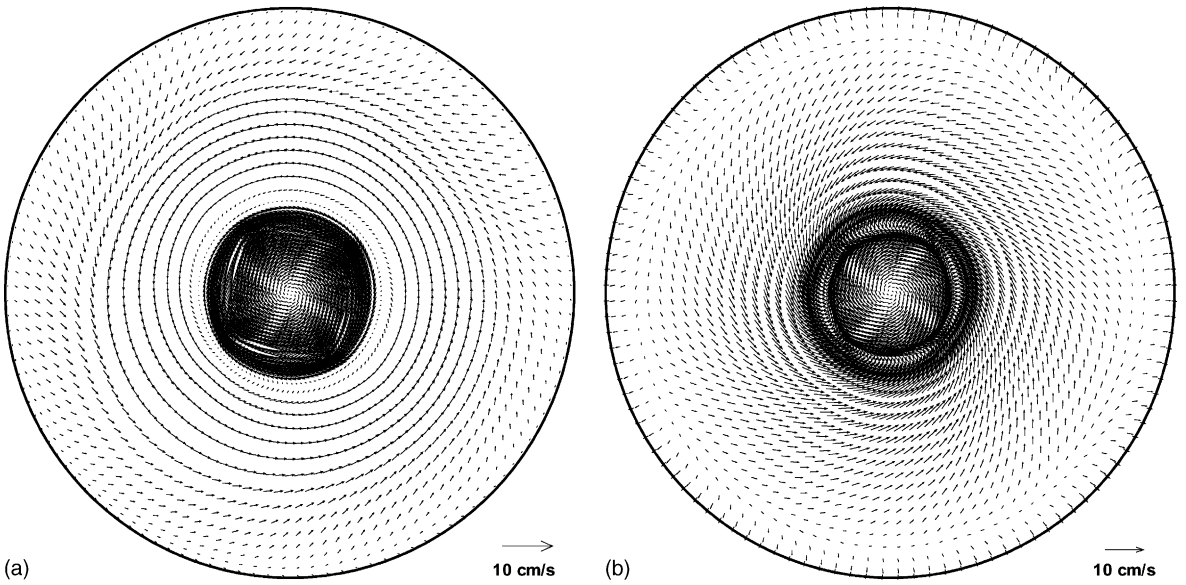

Fig. 7. Time-averaged velocity vectors on a horizontal cut one control volume below the surface: (a) without and (b) with thermocapillary forces.

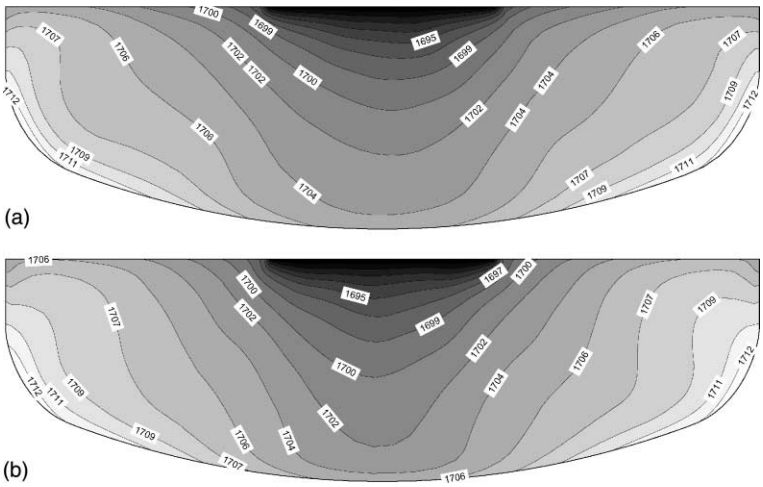

Fig. 8. Time-averaged thermal field on a vertical cut through the crucible (a) without and (b) with thermocapillary forces.

wall as well. As mentioned earlier, the higher temperature gradients exists around the periphery of the rotating crystal in the presence of surface tension forces. This can be clearly observed from the concentrated isotherms around the crystal. Better control of the diameter of the growing crystal can be achieved as a consequence of the formation of the concentrated isotherms. In the case with thermocapillary convection, the higher radial velocity is likely to enhance the convection coefficient and thereby the heat transfer. However, owing to the low *Pr* of the melt, the liquid temperature below the crystal does not show appreciable differences for the cases with and without thermocapillary convection. Although computations have been carried out with a fixed flat shape of the crystal-melt interface, it can be concluded that the thermocapillary convection influences the growth of the crystal due to the increased heat flux at the growth interface. This influence is more significant in the case of high-*Pr* fluids [12,19].

Fig. 9 shows the azimuthal and time-averaged temperature distribution $\overline{T}$ at two different melt heights for the cases with and without the effect of thermocapillary forces. It can be observed that below the free surface, the fluid is hotter at both positions for the case when the thermocapillary effect is included. This is primarily due to the high-velocity surface flow from the crucible walls to the center of the melt. Therefore, the vertical temperature gradient at the level of the free surface is decreased in the presence of the thermocapillary effect. Near the periphery of the rotating crystal, this effect is maximized. From the above discussions it is discerned that the surface tension driven flow shrinks the colder region around the crystal. At the free surface, thermocapillary force strengthens the buoyancy driven force by inducing a flow from the crucible wall towards the growing crystal.

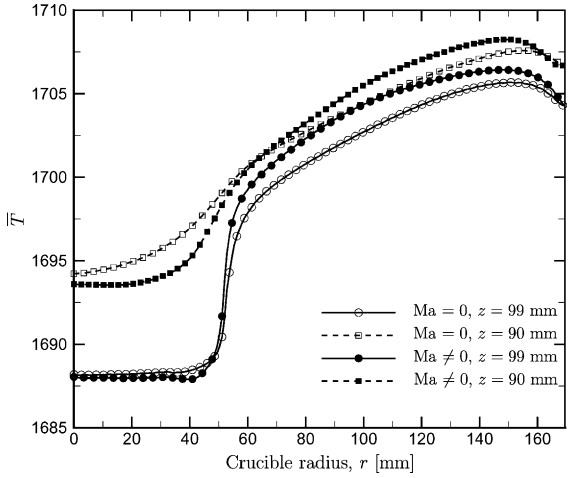

Fig. 9. Azimuthal- and time-averaged temperature $\overline{T}$ plotted at two different melt heights for the cases with and without thermocapillary forces.

5.3. Fluctuating velocity and temperature fields

The Rayleigh–Bérnard instability in a melt arises owing to the presence of a cooler layer of the fluid above a warmer layer. The cooler layer is referred to as an *unstable layer* [33]. The thermocapillary convection increases the temperatures of both layers. Moreover, the temperature difference between the same two layers is reduced (see Fig. 9). It can be inferred that for the reasons stated above, the temperature fluctuations subside at the free surface. This can be seen from Fig. 10, which shows the root mean square (rms) temperature fluctuations (averaged in the azimuthal direction) at two different heights in the melt for the cases with and without Marangoni convection. Immediately below the crystal

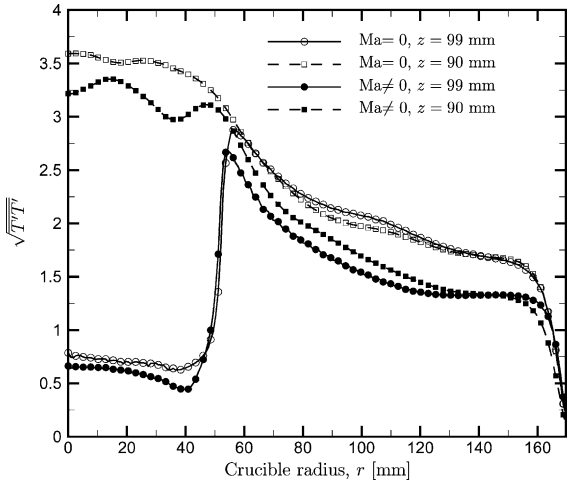

Fig. 10. Root mean square of temperature fluctuations at two different melt heights for the cases with and without the thermocapillary effect.

and the free surface, the temperature fluctuations are also decreased for the case when thermocapillary force is superimposed whereas the velocity fluctuations (the kinetic energy of turbulence, k) are intensified, as shown in Fig. 11. However, Fig. 11 reveals that the velocity fluctuations under the free surface are reduced in the presence of the thermocapillary effect. This trend is in contrast to what is observed in the region underneath the crystal. The reason for this trend can be attributed to the decreased vertical temperature gradient below the free surface due to the presence of the thermocapillary effect as mentioned earlier. The Marangoni effect enhances the net inward radial flow, leading to better thermal mixing and lower temperature fluctuations. The position of the maximum rms temperature fluctuations reveals a correlation with the position of the maximum radial gradient of the average temperature.

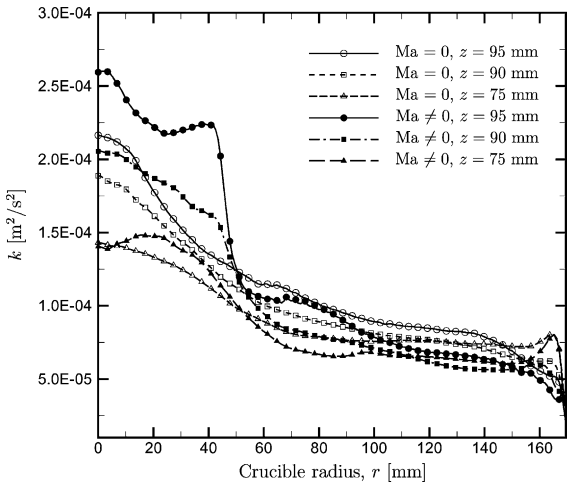

Fig. 11. Azimuthal- and time-averaged kinetic energy of turbulence k at different melt heights for the cases with and without thermocapillary convection.

6. Conclusions

Numerical simulations were performed in order to investigate the influence of thermocapillary forces on the time-averaged and instantaneous velocity and temperature fields in an industrial Cz crucible for Si growth. Owing to the presence of the thermocapillary effect, the following significant observations were made.

- The thermocapillary forces increase the inward radial velocity on the free surface of the melt. The inward radial flow near the free surface completely surpasses the flow due to the centrifugal force near the periphery of the rotating crystal.
- The results indicate the presence of Rayleigh–Bérnard instabilities and the time-dependent nature of the melt. The presence of high-temperature gradients or the concentration of the isotherms around the crystal edge due to the strong thermocapillary flow towards the cold crystal ensures better control of the diameter of the growing crystal.
- The regions underneath and around the crystal become cooler owing to the enhanced flow induced by the thermocapillary convection. The surface tension induced flow promotes deep penetration of the temperature fronts inside the melt and reduces the radial temperature gradients along the free surface of the melt. On the other hand, the temperature of the free surface layer is increased owing to enhanced flow velocity towards the crystal from the side hot walls.
- The net radial mass flow rate near the crystal is enhanced by thermocapillary driven flow and this brings about better mixing. As a consequence, the temperature fluctuations are reduced at the crystal interface, while turbulent kinetic energy is increased underneath the crystal interface.
- Owing to decreased vertical temperature gradients below the free surface, the amplitudes of the temperature and velocity fluctuations are reduced near the free surface of the melt.

The results clearly indicate that even in low-Pr melts, the thermocapillary effect is important and may significantly affect the quality of the crystal by influencing the turbulent transport of heat and mass near the growing crystal. As the crystal grows in size, the melt volume in the crucible decreases. The height of the melt decreases and the effect of the thermal buoyancy force becomes weaker than the effect of the thermocapillary force. In

such a situation, the importance of Marangoni convection in a numerical simulation becomes further intensified.

Acknowledgements

The simulations were carried out on the Fujitsu VPP 700 of Leibniz Computer Center (LRZ), Munich, and the Fujitsu VPP 300 of Regional Computing Center (RRZE), Erlangen. This support is gratefully acknowledged. The stay of Prof. Gautam Biswas at LSTM was supported by KONWIHR and DAAD. Finally, we thank Dr. Biswajit Basu, TRDDC, Pune, India, and Mr. Frank Schäfer of LSTM, Erlangen, for helpful discussions.

References

[1] K. Kakimoto, M. Eguchi, H. Watanabe, T. Hibiya, Natural and forced convection of molten silicon during Czochralski single crystal growth, J. Crystal Growth 94 (1989) 412–420.
[2] N. Kobayashi, Steady state flow in a Czochralski crucible, J. Crystal Growth 147 (1995) 382–389.
[3] A.D.W. Jones, Scaling analysis of the flow of a low Prandtl number Czochralski melt, J. Crystal Growth 88 (1988) 465–476.
[4] S.M. Pimputkar, S. Ostrach, Convective effects in crystal growth from melt, J. Crystal Growth 55 (1981) 614–646.
[5] J.R. Ristorcelli, J.L. Lumley, Instabilities transition and turbulence in the Czochralski crystal melt, J. Crystal Growth 116 (1992) 447–460.
[6] A. Lipchin, A.R. Brown, Comparison of three turbulence models for simulation of melt convection in Czochralski crystal growth for silicon, J. Crystal Growth 205 (1999) 71–91.
[7] T. Azami, S. Nakamura, M. Eguchi, T. Hibiya, The role of surface-tension-driven flow in the formation of surface pattern on a Czochralski silicon melt, J. Crystal Growth 233 (2001) 99–107.
[8] D. Schwabe, J. Metzger, Coupling and separation of buoyant and thermocapillary convection, J. Crystal Growth 97 (1989) 23–33.
[9] D. Schwabe, A. Scharmann, Marangoni convection in open boat and crucible, J. Crystal Growth 52 (1981) 435–449.
[10] C.J. Jing, N. Imaishi, S. Yasuhiro, Y. Miyazawa, Three-dimensional numerical simulation of spoke pattern in oxide melt, J. Crystal Growth 200 (1999) 204–212.
[11] C.J. Jing, N. Imaishi, T. Sato, Y. Miyazawa, Three-dimensional numerical simulation of oxide melt flow in the Czochralski configuration, J. Crystal Growth 216 (2000) 372–388.
[12] Z. Galazka, H. Wilke, Influence of Marangoni convection on the flow pattern in the melt during growth of $Y_3Al_5O_{12}$ single crystals by the Czochralski method, J. Crystal Growth 216 (2000) 389–398.
[13] P. Hintz, D. Schwabe, H. Wilke, Convection in a Czochralski crucible–Part 1: non-rotating crystal, J. Crystal Growth 222 (2001) 343–355.
[14] P. Hintz, D. Schwabe, Convection in a Czochralski crucible—Part 2: rotating crystal, J. Crystal Growth 222 (2001) 356–364.
[15] K. Yi, K. Kakimoto, M. Eguchi, M. Watanabe, T. Shyo, T. Hibiya, Spoke patterns on molten silicon in Czochralski system, J. Crystal Growth 144 (1994) 20–28.
[16] T. Zhang, G.X. Wang, H. Zhang, F. Ladeinde, V. Prasad, Turbulent transport of oxygen in the Czochralski growth of large silicon crystals, J. Crystal Growth 198/199 (1999) 141–146.
[17] K. Kakimoto, H. Ozoe, Oxygen distribution at a solid–liquid interface of silicon under transverse magnetic fields, J. Crystal Growth 212 (2000) 429–437.
[18] M. Li, Y. Li, N. Imaishi, T. Tsukada, Global simulation of a silicon Czochralski furnace, J. Crystal Growth 234 (2002) 32–46.
[19] D. Lamprecht, D. Schwabe, A. Scharmann, E. Schultheiss, Experiments on buoyant, thermocapillary and forced convection in Czochralski configuration, J. Crystal Growth 65 (1983) 143–152.
[20] A. Hirata, T. Fukuda, Observation of crystal-melt interface shape in simulated Czochralski methods with model fluid, J. Crystal Growth 128 (1995) 195–200.
[21] C. Wagner, R. Friedrich, DNS of turbulent flows in idealised Czochralski crystal growth configurations, in: Computation and Visualization of Three-Dimensional Vortical and Turbulent Flows, Vieweg Verlag, 1996, pp. 172–190.
[22] C. Wagner, Direct Navier–Stokes simulations of turbulent Czochralski flows, in: High Performance Scientific and Engineering Computing, Lecture Notes in Computational Science and Engineering, Springer, 1998, pp. 279–292.
[23] B. Basu, S. Enger, M. Breuer, F. Durst, Three-dimensional simulation of flow and thermal field in a Czochralski melt using a block-structured finite-volume method, J. Crystal Growth 219 (2000) 123–143.
[24] O. Gräbner, G. Müller, J. Virbulis, E. Tomzig, Effects of various magnetic field configurations on temperature distribution in Czochralski silicon melts, Micro. Engng. 56 (2001) 83–88.
[25] W. Rhim, K. Oshaka, Thermophysical properties measurement of molten silicon by high-temperature electrostatic levitator: density, volume expansion, specific heat capacity, emissivity, surface tension and viscosity, J. Crystal Growth 208 (2000) 313–321.
[26] C.E. Chang, W.R. Wilcox, Inhomogeneities due to thermocapillary flow in floating zone melting, J. Crystal Growth 28 (1975) 8–12.
[27] J.H. Ferziger, M. Perić, Computational Methods for Fluid Dynamics, Springer, Berlin Heidelberg, 1999.
[28] S. Patankar, D. Spalding, A calculation procedure for heat, mass and momentum transfer in three-dimensional parabolic flows, Int. J. Heat Mass Transfer 15 (1972) 1787–1806.
[29] H.L. Stone, Iterative solution of implicit approximations of multidimensional partial differential equations, SIAM J. Numer. Anly. 5 (1968) 530–558.
[30] F. Durst, M. Schäfer, K. Wechsler, Efficient simulation of Incompressible viscous flows on parallel computers, Notes Numer. Fluid Mech. 38 (1993) 79.

[31] S. Enger, M. Breuer, B. Basu, Numerical simulation of fluid flow and heat transfer in an industrial Czochralski melt using parallel-vector supercomputer, in: Numerical Lecture Notes in Computational Sciences and Engineering, 1999.

[32] B. Cabral, L. Leedom, Imaging vector fields using line integral convolution, In: Computer Graphics Proceedings, vol. 27.4, Annual Conference Series, Los Angeles, CA, July 1993, ACM SIGGRAPH, Addison-Wesley, pp. 263–270.

[33] K.W. Yi, V.B. Booker, M. Eguchi, T. Shyo, K. Kakimoto, Structure of temperature and velocity fields in the Si melt of a Czochralski crystal growth system, J. Crystal Growth 156 (1995) 383–392.